BNL-82219-2009-JA

Atmos. Chem. Phys. Discuss., 9, 12027–12064, 2009
www.atmos-chem-phys-discuss.net/9/12027/2009/
© Author(s) 2009. This work is distributed under
the Creative Commons Attribution 3.0 License.

Atmospheric Chemistry and Physics Discussions

This discussion paper is/has been under review for the journal *Atmospheric Chemistry and Physics (ACP)*. Please refer to the corresponding final paper in *ACP* if available.

Retrieval of cloud liquid water distributions from a single scanning microwave radiometer aboard a moving platform – Part 1: Field trial results from the Wakasa Bay experiment

D. Huang[1], A. Gasiewksi[2], and W. Wiscombe[1,3]

[1]Brookhaven National Laboratory, Upton, NY 11973, USA
[2]University of Colorado, Boulder, CO 80309, USA
[3]NASA Goddard Space Flight Center (code 913), Greenbelt, MD 20771, USA

Received: 14 April 2009 – Accepted: 4 May 2009 – Published: 15 May 2009

Correspondence to: D. Huang (dhuang@bnl.gov)

Published by Copernicus Publications on behalf of the European Geosciences Union.

Abstract

Tomographic methods offer a new promise for retrieving three-dimensional distributions of cloud liquid water from path-integrated radiometric measurements by passive sensors. A mobile cloud tomography system using only a single scanning microwave radiometer has many advantages over a fixed system using multiple distinctly-located radiometers, e.g., efficient and flexible data collection. Part 1 (this paper) examines the results from a limited cloud tomography trial carried out during the 2003 AMSR-E validation campaign at Wakasa Bay of the Sea of Japan. During the tomographic test, the Polarimetric Scanning Radiometer (PSR) and Microwave Imaging Radiometer (MIR) aboard the NASA P-3 research aircraft scanned through a system of low-level clouds and thus provided a useful dataset for testing the cloud tomography method. We conduct three retrieval runs with a constrained inversion algorithm using, respectively the PSR, MIR, and combined PSR and MSR data. The liquid water paths calculated from the PSR retrieval are consistent with that from the MIR retrieval. The retrieved cloud field based on the combined data appears to be physically plausible and consistent with the cloud image obtained by a cloud radar. It is unfortunate that there were no in-situ cloud measurements during the experiment that can be used to quantitatively validate the tomographic retrievals. Nevertheless, we find that some vertically-uniform clouds appear at high altitudes in the retrieved fields where the radar image shows clear sky. This is likely due to flawed data collection geometry, which, in turn, is determined by the radiometer scan strategy, and aircraft altitude and moving speed. This sets the stage for Part 2 of this study that aims at possible improvements of the mobile cloud tomography approach by a group of sensitivity studies using observation system simulation experiments.

1 Introduction

The study of climate and climate change has long been hindered by a lack of information on the effect of clouds on the radiation balance of the earth, especially by a lack of knowledge of spatial distributions of cloud (Ramanathan et al., 1989). The cloud microwave tomography technique that permits the retrieval of cloud liquid water distributions from radiometric measurements was first presented by Warner et al. (1985). It was proposed that the structure of cloud liquid water can be derived by probing the cloud's thermal emission from multiple directions at distinct locations. A certain degree of intersection between microwave beams is necessary for the cloud tomography method to be successful. The first of the several proposed configurations requires the atmospheric emission at a frequency of 31.6 GHz be measured by multiple ground-based radiometers that are located in distinct locations (Fig. 1a). Warner et al. (1986) used this configuration to estimate the liquid water distributions of cumulus clouds, although in six weeks of scanning at Boulder in Colorado only one cloud passed between the two radiometers that could yield a credible tomographic retrieval.

Another more flexible configuration discussed by Warner et al. (1985) is shown schematically in Fig. 1b. An aircraft carries a single radiometer, which switches automatically between two fixed antennas, along a horizontal line passing just under a cloud. The scanning of the dual antennas in different locations provides similar measurements as the angular scanning of the dual ground-based instruments. A theoretical study of this configuration was presented by Drake and Warner (1988) and showed that the configuration with two fixed antennas performed similarly as the ground-based dual-radiometer configuration. A follow-up field test was carried out in Louisiana and the liquid water content (LWC) deduced from the radiometric measurements showed statistically good agreement with that measured directly by an airborne Particle Measurement System (Warner and Drake, 1988).

There were many limitations that prevented the practical use of cloud tomography in 1980s. Chief among them are high cost and huge size of radiometers, slow scanning,

and immaturity of cloud models. We can bring many more resources to bear upon the problem of cloud tomography than in Warner's day, e.g., faster computers, better cloud models, and more advanced mathematical tools. Microwave technologies have also advanced considerably and microwave radiometers have become more portable and reliable while costs have fallen, owing to the commercialization of microwave remote sensing. The reduction in radiometer size with increasing reliability finally makes airborne scanning microwave radiometers reachable for the community. Now is timely to take advantage of the theoretical and technical advances and to extend the cloud tomography technique theoretically and experimentally for more practical applications.

Huang et al. (2008a,b) started the theoretical re-examination of the cloud tomography method after its two-decade dormancy by investigating the mathematical nature of the retrieval problem of ground-based cloud tomography and developing appropriate retrieval algorithms. The first paper rigorously examined the underlying mathematical problem using observation system simulation experiments based on large eddy simulation. It was revealed that, like other limited angle tomography problems, the mathematical problem of the cloud tomography with limited number of ground radiometers (2–4) is highly ill-posed. Its solution is non-unique and very sensitive to measurement noises and numerical errors. The second paper then focused on the development of tomographic retrieval algorithms that make use of various types of constraints based on a priori knowledge to improve the retrieval of ill-posed cloud tomography problems. It was revealed that the use of appropriate constraints can improve the accuracy of the tomographic retrieval by one order.

The ground-based cloud tomography configuration has the advantage of collecting data without human intervention and thus is suitable for long-term cloud observation. For field studies that require more efficient and flexible data collection, the airborne version of cloud tomography is superior to the ground-based configuration. But the airborne configuration with dual antennas (Fig. 1b) also has its limitations that prevent its practical applications, e.g., very limited observing angles and technical difficulties in building such dual-antenna radiometers. The new generation of scanning radiome-

ters developed by the NOAA-CU Center for Environmental Technology at University of Colorado at Boulder, called Polarimetric Scanning Radiometer (PSR), provides a good opportunity to re-evaluate the capability of the air-borne cloud tomography method with state-of-the-art microwave techniques. The PSR was boarded on the NASA P-3 research aircraft along with several other microwave remote sensing instruments during the 2003 Advanced Microwave Scanning Radiometer for EOS (AMSR-E) validation campaign at Wakasa Bay of the Sea of Japan. For only one day (28 January 2003), the PSR was operated in the along-track scanning mode, the only mode that provides appropriate observational geometry for cloud tomography retrieval.

In Part 1 (this paper) we examine the results from the limited cloud tomography trial during the 2003 AMSR-E validation campaign in which the PSR scanned through a system of low-level cloud layers. In Part 2, we then conduct a group of observation system simulation experiments of the mobile cloud tomography system and present several recommendations on how to improve the mobile system.

The paper is organized as follows. Section 2 provides a detailed description on the data collected during the Wakasa Bay experiment. Section 3 sets up the theoretical basis of the tomographic inversion problem. Section 4 elaborates the retrieval procedures. Section 5 presents the retrieval results and also focuses on validation of the tomographic retrievals. Section 6 summarizes the findings of this paper.

2 Data

The data used in this study were collected during the 2003 AMSR-E validation campaign at Wakasa Bay from the instrumented NASA P-3 research aircraft. The instruments include a PSR with multiple working frequencies from 10.7 to 89 GHz, a high frequency Microwave Imaging Radiometer (MIR) covering the spectral range from 89 to 340 GHz, and an Airborne Cloud Radar (ACR) operating at the 95 GHz frequency.

2.1 Description of the Wakasa Bay field campaign

The 2003 Wakasa Bay field campaign was a cooperative effort between the Japan Aerospace Exploration Agency (JAXA), AMSR precipitation validation team, and the NASA AMSR-E team focusing on the physical validation of shallow snowfall and rainfall retrievals from the AMSR and AMSR-E (Lobl et al., 2007). Wakasa Bay, on the eastern end of the Sea of Japan, has fairly predictable cold air outbreaks during winter time in which cold air from the Eurasian continent blows over the relatively warm Sea of Japan. These storms typically produce very shallow rainfall layer near the surface, where warm boundary layer air mixes with the cold air aloft.

The validation campaign collected a wealth of now publicly available in situ and remotely sensed data of low- and mid-altitude winter clouds and precipitation from 14 January 2003 to 3 February 2003. The observations collected during this experiment include ground and airborne radar reflectivities, microwave brightness temperatures, and in situ data intended to extend our understanding on winter precipitation over mid-latitude ocean. To test the validity of the airborne cloud tomography method, we select the data obtained on 28 January 2003 within a 176-km long flight line starting from (37.525° N, 133.522° E) to (38.8° N, 134.792° E) (Fig. 2), where the PSR was programmed to scan in the along-track mode – the only mode that provides appropriate observational geometry for the purpose of cloud tomography retrieval during this validation campaign (see more details in Sect. 2.2).

2.2 Polarimetric Scanning Radiometer

The PSR developed by the Center for Environment Technology of University of Colorado at Boulder is a versatile microwave imaging radiometer for the purpose of obtaining polarimetric microwave emission imageries of the Earth's oceans, land, ice, clouds, and precipitation. The PSR provides vertical and horizontal polarization measurements from C-band to W-band frequencies (Piepmeier and Gasiewski, 1996). The basic concept of the PSR is a set of polarimetric radiometers housed within a gimbal-

mounted scanhead drum. The scanhead drum is rotatable by the gimbal positioner so that the radiometers can view any angle within ±70° elevation off nadir at any azimuthal angle (a total of 1.32 sr solid angle), as well as external hot and ambient calibration targets. The PSR configuration was operated in various scanning modes including conical, cross-track, along-track, fixed-angle stare, and spotlight modes, but only the along-track data provides acceptable amount of intersecting beams that are necessary for tomographically retrieving the spatial distribution of cloud liquid water. Figure 3 shows the swaths of three successive PSR along-track scans; each scan cycle covers an isosceles-trapezoid-shaped region whose base angle is 20 degrees and the distance between two successive scan cycles is approximately 5.85 km. Note that the swath of each scan cycle is shown in different color. The lower parts of two successive scans have significant overlap with each other, while there is almost no overlap at high altitudes. Furthermore, a scan has a little overlap with its second successive scan and no overlap with its third successive scan (even at low altitudes). As it will be shown later in this paper, the poor overlap between the swaths of scan cycles sets a serious limit on the capability of the mobile cloud tomography method to reproduce small-scale cloud structure.

A suite of Matlab programs, developed by the NOAA-CU Center for Environment Technology of University of Colorado at Boulder, were used to extract and calibrate the radiometric data. The first step is decoding the navigation information such as geographic coordinate, altitude, yaw, roll, and pitch of the platform from the recorded navigation data. Then the radiometric data are partitioned into individual "maneuvers" based on the navigation information – a maneuver is a segment of flight during which the aircraft keeps the same altitude and orientation and the radiometer remains in the same scanning mode. The calibration algorithm described in Corbella et al. (2002) was used to convert the raw data into microwave brightness temperatures. The calibration method consists of periodically switching the receivers' input to a noise diode and infrequent viewing two external reference targets. The gain and offset at closely spaced time intervals are computed using the noise diodes, but referring the diodes'

noise temperatures to precise measurements of the external targets.

The original radiometric data were recorded with 7.5 ms integration time, resulting in about 8000 beams per one-minute scanning. The 7.5 ms integration time corresponds to a 0.03 degree angular increment between two successive beams. Given the 2.3-degree antenna beam width, the actual beam volumes of any two successive beams are 99% overlapped and thus the redundancy in the original data is very high. We thus average the original data to 150-ms resolution not only to reduce the total volume of the data but also to dampen the random noise in the data.

Figure 4a shows the mean brightness temperatures at the 37 GHz frequency averaged over horizontal and vertical polarizations as a function of distance (or, equivalently, UTC time). The brightness temperatures range from 160 K to 220 K. Figure 4b shows that the corresponding view angles range from 200 degrees (70 degrees off nadir in the forward direction) to 340 degrees (70 degrees off nadir in the backward direction). Periodical observation gaps are noticeable in the data. These gaps correspond to the part of PSR scan cycles that no atmosphere measurements were made when the scanhead was viewing or proceeding for viewing the external blackbody calibration targets.

2.3 Microwave Imaging Radiometer

The MIR is a nine-channel air-borne imaging radiometer that is designed to fly aboard high altitude aircrafts for atmospheric research (Racette et al., 1996). Three dual pass band channels are centered about the strongly opaque 183 GHz water absorption line and a fourth channel is located at 150 GHz. These channels have varying degrees of opacity from which the water vapor profile can be inferred. There are two additional channels located at 89 GHz and 220 GHz. During the Wakasa Bay field campaign, the imager was programmed to scan across the flight track with a 106° swath centered about nadir with a 3.5-degree beamwidth. In every scan cycle of about 3 s, it views two external calibration targets in addition to the 106-degree scene scan; one of these targets is heated to a temperature of 330 K and the other remains at the ambient

temperature of the aircraft cruising altitude.

The MIR measurements from the Wakasa Bay field campaign were calibrated by the Microwave Sensors Branch of NASA/Goddard Space Flight Center and were made available at National Snow and Ice Data Center (NSIDC) (Wang et al., 2004). We use only the cross-track nadir-looking beams. The reason for using only the nadir beams is that these beams are within the PSR along-track scanning plane and thus can serve as a useful supplement to the along-track PSR data that contain many observation gaps (each 1–3 km long, as shown in Fig. 4a). To minimize the complexity caused by scattering of ice particles, we use the lowest frequency of MIR, i.e., the 89 GHz channel.

Figure 4c shows the MIR nadir brightness temperatures at 89 GHz frequency. The minimum brightness temperatures observed by MIR is 195 K, possibly corresponding to a clear sky condition; the maximum value observed is 250 K, indicating the presence of a moderately thick cloud. The MIR brightness temperatures at 89 GHz, on average, are about 30 K higher than those of the PSR at 37 GHz. This is not surprising because of a higher emission efficiency of cloud liquid water at 89 GHz and also higher sea surface thermal emission at this frequency.

2.4 Airborne Cloud Radar

The ACR is a scanning Doppler cloud radar capable of providing co- and cross-polarization radar reflectivities at a frequency of 95 GHz with a 0.56° beamwidth (Sadowy et al., 1997). It was designed as a prototype airborne facility for the development of the Cloud Profiling Radar System, which is the central instrument for NASA CloudSat mission. The ACR can operate in both a fixed (downward and upward looking, nadir parallel) and scanning mode (vertical scanning, various degree intervals off nadir).

During the Wakasa Bay field campaign, the ACR was operated in the fixed downward looking mode. The ACR provides independent measurements of two-dimensional cloud structure along the flight track. So the ACR data can be used to evaluate the tomographic retrievals from the passive measurements of microwave radiometers. The

ACR data used in this study were processed by the Department of Atmospheric Science of Colorado State University. Figure 5 shows a 2-D snapshot of radar reflectivity factors obtained within the flight line shown in Fig. 2. The radar reflectivity factors range from −40 dBZ (clear sky) to 40 dBZ (sea surface return). The maximum reflectivity found in clouds is 15 dBZ, suggesting that a significant amount of large particles such as rain and ice were present in the clouds. No bright band (melting layer which appears to be brighter to the radar than neighboring layers) is found in the image. This is consistent with the dropsonde measurements that the air temperature at the surface level is close to the freezing point (more details at Sect. 2.5).

2.5 Dropsonde data

Various types of radiosondes have been widely used to make direct in-situ measurements of air temperature, humidity and pressure with height, typically to altitudes of approximately 30 km. During the cloud tomography experiment, there was a dropsonde launch every 10–15 min from the NASA P-3 aircraft. Three of them were within the 176-km long flight line shown in Fig. 2. We average the data from these three dropsondes to obtain the mean profiles of atmospheric temperature and humidity. Figure 6 shows the mean profiles of air temperature and water vapor mixing ratio. The air temperature is close to zero degree Celsius near the surface and decreases to −25 degrees at the altitude of 4.1 km (no dropsonde data available above this level). The relative humidity is 63% at the surface level, increases steadily to its maximum value of 92% at the altitude of 1.5 km, and falls gradually to less than 10% at 4 km. The lifting condensation level and adiabatic cloud water content then can be easily calculated from the mean atmospheric profiles.

3 Theoretical basis of the inversion problem

The radiation intensity, usually expressed as brightness temperature, recorded by microwave radiometers, is related to the spatial distribution of cloud water content and other atmospheric variables through a one-dimensional radiative transfer equation without the scattering term (since cloud droplets appear to be very close to blackbody in the microwave region). Given a total number of m microwave rays, the 1D radiative transfer equation can be discretized by dividing the retrieval domain into $n=N^3$ (N^2 for a 2-D slice) equal- sized pixels to yield the following matrix equation:

$$\boldsymbol{Ax} = \boldsymbol{b}\,, \tag{1}$$

where $\boldsymbol{x}^T=(\alpha_1, \alpha_2, \cdots, \alpha_n)$ is the vector of atmosphere absorption coefficients (includes contributions from cloud water, water vapor, and oxygen); $\boldsymbol{b}^T=(b_1, b_2, \cdots, b_m)$, is the vector of adjusted microwave measurements; and $\boldsymbol{A}=(a_{ij})$, also called kernel matrix, is an $m\times n$ matrix that approximates the radiative transfer operator discretely.

The tomographic retrieval problem now becomes the inversion of the matrix Eq. (1) for the vector of absorption coefficients and then the absorption coefficients can be easily converted into cloud water content (Warner et al., 1985; Huang et al., 2008a). While a direct application of the conventional least squares method to an ill-posed problem like cloud tomography would result in large errors in the solution, regularization techniques are usually needed to reduce the sensitivity of the solution to measurement noises and numerical errors (Twomey, 1977). In our previous studies, we adapted the Tikhonov regularization technique to make use of a variety of constraints. The inclusion of constraints greatly reduces the retrieval sensitivity to noises and numerical errors and thus obtains a better retrieval for the ill-posed tomographic retrieval problem. The idea is to seek the appropriate vector $\boldsymbol{x}$ for the following constrained minimization problem:

$$\min_x \left\{ \|\boldsymbol{Ax} - \boldsymbol{b}\|_2^2 + \lambda \|\boldsymbol{Lx}\|_2^2 \right\}\,, \tag{2}$$

where $\lambda \|\boldsymbol{Lx}\|_2^2$ is the regularization term, $\|\bullet\|_2$ stands for the Hilbert L_2 norm, $\boldsymbol{L}$ is the regularization matrix and usually takes the form of a discrete approximation of the spatial derivative operator, and λ is the regularization parameter determining the amount of the smoothness to be imposed on the retrieval. It is known that regularization techniques in the form of an L_2 norm, e.g., the Tikhonov regularization, tend to bias toward a smooth solution (Strong and Chan, 2003). This is confirmed by one of our previous study that shows the Tikhonov method often fails to capture some discontinuous structures, e.g., the retrieval cannot reproduce the sharp edges at cloud top and instead the retrieved cloud top boundaries are often blurred and extended to higher altitudes (Huang et al., 2008b).

In order to improve the retrieval of discontinuous structures, non-linear regularization techniques in the form of L_1 norm like the total variation (TV) regularization have been proposed in image restoration applications (Acar and Vogel, 1994; Chambolle and Lions, 1997):

$$\min_x \left\{ \|\boldsymbol{Ax} - \boldsymbol{b}\|_2^2 + \lambda \|\boldsymbol{Lx}\|_1 \right\}\,. \tag{3}$$

For the total variation regularization, the regularization term can be written as $\|\boldsymbol{Lx}\|_1 = TV(\boldsymbol{x}) \equiv \sum_i |\nabla x_i| \Delta r \equiv \sum_i \left| \left(\frac{\partial}{\partial h} + \frac{\partial}{\partial v}\right) x_i \right| \Delta r$, where r denotes the spatial coordinate, Δr stands for the area or volume of an individual pixel and can usually be neglected in practical computation, h and v, respectively denote the horizontal and vertical directions. A more detailed discussion on the choice of the regularization term will be presented in the part II of this paper. The main advantage of the L_1 norm total variation regularization is that it doesn't penalize discontinuities in the solution, while simultaneously not penalizing smoothness in the solution; thus under certain conditions it can preserve the exact discontinuous edges in the solution (Acar and Vogel, 1994; Strong and Chan, 2003). The implementation of such L_1 norm regularization techniques is more difficult than the L_2 norm techniques because of the non-linearity of the L_1 norm regularization term.

In this research, several other constraints beside the smoothness constraint are also used in the retrieval algorithm. First, to better capture the adiabatic or sub-adiabatic distribution of cloud water in the vertical direction, we make a small modification to the regularization term shown in Eq. (3). The new regularization term is now written as: $\|\boldsymbol{Lx}\|_1 = \sum_i |\nabla x_i| \Delta r \equiv \sum_i \left| \left(\frac{\partial}{\partial h} + \frac{\partial}{z \partial v} \right) x_i \right| \Delta r$, where z stands for the central height of the volume Δr. This constraint will usually drive the vertical distribution of retrieved cloud water toward an adiabatic shape. Second, a non-negative constraint is included to meet the apparent physical requirement that all retrievals must be non-negative. The non-negative constraint was also used in our previous cloud tomography retrieval algorithms. Last, a support constraint is imposed to the retrieval; the support constraint forces the retrieval to vanish outside a pre-determined support region S. The use of the support constraint is necessary since some knowledge on cloud boundaries is usually available either from a radar image or from the atmospheric temperature and humidity profiles. More details on the implementation of these constraints are provided later in this section.

A major difficulty of all the regularization techniques is to determine the weight of each regularization term, in other worlds, to determine how much information in the retrieval should come from the regularization. Usually the weighting parameter λ is determined either in an ad hoc manner based on a priori knowledge or in an iterative manner by performing the inversion many times with different regularization parameters and choosing the appropriate regularization parameter based on the L-curve or the cross-validation method. This iterative method for choosing the regularization parameter is computationally expensive and sometimes is difficult to apply in operational algorithms. In many practical applications, there is an estimate about the uncertainties in the measured data and in the forward model, and this information can be used to choose the regularization parameter. To do this, here we reformulate the regularization problem in a slightly different way with the formulations of Eqs. (2) and (3). For the total

variation regularization, the new formulation is:

$$\min_x \{\|\boldsymbol{Lx}\|_1\}, \text{ subject to } \|\boldsymbol{Ax} - \boldsymbol{b}\|_2^2 \leq \varepsilon \text{ and other constraints.} \quad (4)$$

Here ε stands an the error tolerance. Hansen (1998) pointed out that for any choice of ε in Eq. (4) there always exists a regularization parameter λ that the formulation Eq. (2) will yield the same solution as Eq. (4).

The constrained inversion problem (Eqs. 1–4) can be solved by a direct inversion method, i.e., the method involving the calculation of the inverse of the kernel matrix. The direct method is fast and works well when the dimensionality of the problem is not large. The computational time usually increases with $O(n^2)$; thus for very high-dimensionality problem the direct method will be very slow sometimes even impossible because the size of the kernel matrix will get unmanageable. In contrast, for an iterative method like the algebraic reconstruction algorithm (Gordon et al., 1979), a widely used technique in many tomographic applications, the computational cost increases only linearly with the dimensionality of the problem ($O(n)$). Therefore, it has a great advantage over the direct method for large dimensional problems. In this study, we choose the iterative method because of the large number of radiometric measurements (about 10 000 beams with a 150-ms averaging).

Figure 7 shows the pseudo-code that implements the algorithm Eq. (4) and it is a modification of the algorithm proposed by Sidky et al. (2008). The aim is to minimize the total variation of the retrieval subject to several constraints including the data constraint, the non-negativity constraint, and the support constraint. The total variation term is minimized by a steepest descent method with an adaptive step-size d_{TV}. The other constraints are enforced by the use of projection onto convex sets (POCS) (Youla and Webb, 1982; Sezan and Stark, 1982, 1983). The POCS projection operator for the data constraint, which assures that the predicted measurements $\boldsymbol{Ax}$ is within a specified tolerance ε of the measured data $\boldsymbol{b}$, is chosen to be the simultaneous algebraic reconstruction technique (SART) with a decreasing step size d_{data} (Anderson and Kak, 1982). The non-negativity constraint satisfies the apparent physical requirement that

cloud water content must be non-negative and the corresponding POCS projection operator takes the simple form shown in line 4 (Fig. 7). The support constraint allows the retrieval to be non-zero only in the support region $\boldsymbol{L}$ and its corresponding POCS projection operator is described in line 5 (Fig. 7).

The step-size adaptation of the TV steepest descent is performed at line 10 in such a way as to the change in the retrieval due to the TV steepest descent should be smaller than that due to data constraint. This means the retrieval must first satisfy the data constraint (within the measurement error tolerance) when moving toward other types of constraints. At each step, the step size for the data constraint is dampened by a factor that is slightly smaller than unit. When the change due to the TV steepest descent is larger than that due to the data constraint, the gradient-descent step-size d_{TV} is reduced by a factor that is slightly less than the damping factor for the data constraint. Once the retrieval satisfies the data-tolerance condition as the iteration proceeds, the TV gradient-descent step-size will be no longer reduced, allowing it to become larger than the step-size of data constraint, because the step-size of the data constraint is always decreasing. As a result the retrieval will drift toward lower-TV directions. When the data constraint is violated again, the steepest-descent step-size reduction will continue.

4 Retrieval procedures

Section 3 not only outlines the theoretical basis for retrieving distributions of cloud liquid water from multi-angular microwave emission measurements but also establishes the basis of the constrained retrieval algorithm. In order to use the aforementioned constrained algorithm to solve Eq. (4) for the vector of absorption coefficient, the kernel matrix $\boldsymbol{A}$ and the measurement vector $\boldsymbol{b}$ have to be specified using available data or model simulation.

First, the microwave emission from the underneath sea surface is needed in order to compute the kernel matrix $\boldsymbol{A}$. The microwave signal received by the airborne radiome-

ters is composed of the thermal emission from the atmosphere along the measurement path plus the path-attenuated emission from the underneath sea surface. Therefore, the background emission, i.e., sea surface emission here, has to be specified either through direct measurements (not available in the Wakasa Bay field campaign) or by model simulations. It is well known that sea surface microwave emission is depended not only on the thermodynamic temperature of the sea surface but also on the incident angle. This dependency can be further complicated by waves and foams caused by surface wind. In this study, a two-scale sea surface thermal emission model (Johnson, 2006) is used to estimate the directional variation of sea surface brightness temperature at different spectral frequencies.

Second, in order to retrieve the distribution of cloud LWC in a certain domain using the cloud tomography method, the knowledge of cloud liquid water distribution in its adjacent regions is needed. Some slant beams could pass through both the interested domain and its neighboring regions. The vector $\boldsymbol{b}$ in Eq. (1) should be adjusted so that the contribution by the emission from adjacent regions is removed. Given the aircraft cruising altitude of 6.7 km and the maximum off-nadir scanning angle of 70 degrees, a simple geometrical calculation shows that the cloud liquid water distributions in two 15-km long regions, one north-east and the other south-west to the retrieval domain, are needed to calculate the vector $\boldsymbol{b}$. It is clearly unfortunate that there were no other direct measurements of the cloud liquid water distribution during the experiment that can be used to specify the distribution of cloud liquid water in the two neighboring regions. So we use the ACR radar reflectivity factors at the 95 GHz frequency, combined with a simple sub-adiabatic cloud model, to estimate the distribution of cloud liquid water in the two neighboring regions. It is known that converting radar reflectivity factors to cloud water content using empirical Z-LWC relationships (formulas that convert radar reflectivity into cloud LWC) would be unreliable when the radar data are contaminated by large particles like ice and precipitation (Frisch et al., 1995). Therefore we use the radar data only to determine the cloud top boundary and set the cloud base to be the lifting condensation level that can be determined using the atmospheric profiles

derived from nearby dropsonde descends. Then we use a subadiabatic profile to approximate the vertical distribution of cloud LWC. A subadiabatic profile is characterized by the adiabaticity, defined as the ratio of actual subadiabatic LWP to the adiabatic LWP. As will be discussed later in details, the adiabaticity is a tunable parameter in the retrieval algorithm and it is determined by minimizing the mean difference between the observed and predicted brightness temperatures.

With the background and side boundary emission being specified, the last step is to invert the calibrated radiometric data for the vector $\boldsymbol{x}$ of absorption coefficients (see Eq. 1) using the constrained least squares algorithm described in Sect. 3. The constraint terms in formulation (4) has to been specified. First, we estimate the overall uncertainty in the measured microwave brightness temperature plus the modeled sea-surface brightness temperature to be around 2.0 K. The error tolerance ε is thus set to be $2.0*m$. Second, the cloud top height is around 3.0 km from the radar image (Fig. 5) and this is further confirmed by a temperature inversion observed at 3.1 km (Fig. 6). Conservatively, we thus set the cloud support to be within 3.5 km, that is, cloud water content will be zero above 3.5 km.

With the constraints being specified, the vector $\boldsymbol{x}$ of absorption coefficient can be obtained by the inversion algorithm described in Fig. 7. The cloud absorption coefficient is proportional to cloud LWC and is also depended on the thermodynamic temperature and the mass of cloud liquid water, water vapor, and oxygen (Warner, et al., 1985; Huang et al., 2008a); thus the vertical profiles of air temperature, pressure, and water vapor mixing ratio are needed in order to extract the distribution of cloud LWC from the vector $\boldsymbol{x}$ of absorption coefficient. In this study, these needed profiles are readily obtained from several dropsondes launched during the flight (Fig. 6); thus the distribution of cloud LWC can be easily deduced from the distribution of cloud absorption coefficient.

5 Results and discussions

Our previous studies show that, for a fixed ground-based cloud tomography configuration, the number of radiometers and their physical arrangement determine the geometry of the tomographic data and thus play a critical role in determining the finest spatial scale that a cloud tomography reconstruction can resolve. In the same way, for the airborne tomography system with a single scanning radiometer, the spacing between successive radiometer scan cycles determines the intersection between microwave beams in these cycles and thus should have an important impact on the tomographic retrieval. In order to examine the effects of beam intersection, we perform three retrieval runs: the first run uses only the nadir-viewing beams of the MIR cross-track data (no intersection between beams); the second run uses only the PSR along-track data; and the third run includes both the PSR data and the MIR nadir data. It is clearly unfortunate that no in-situ observations are available with which to quantitatively compare the tomographically-retrieved values of cloud LWC. So we qualitatively evaluate the tomographic retrievals by examining the consistency between the retrievals and the cloud radar image and by comparing the resultant liquid water path (LWP) in the three retrieval runs.

5.1 Retrieval using only the MIR nadir data

The retrieved cloud LWC field for the first run (using only the MIR nadir data) is shown in Fig. 8a. The mean LWC is $0.069\,\mathrm{gm}^{-3}$ and this gives to a mean LWP of $462\,\mathrm{gm}^{-2}$. The retrieved cloud field appears to be vertically uniform at many locations, as one would expect, revealing almost no information about the vertical structure of clouds. Of course, this is not a surprising result because the MIR data used here are nadir-viewing and thus fail to meet the critical requirement of cloud tomography that the microwave beams made at distinct locations must intersect with each other to some extent. Theoretically, only the integrated quantity, LWP, in the along-track vertical plane can be retrieved from these nadir-viewing observations. The horizontal structure of the MIR

LWP shows some consistency with that in the radar image, i.e., some correlation between the LWP and the vertically integrated radar reflectivity. But the MIR retrieval has little cloud water in the regions between 45 to 55 km, 60 to 70 km, and 140 to 150 km where the radar shows very strong returns (5–20 dBZ), indicating the presence of large particles such as ice. This is likely due to the scattering of ice in these regions that suppresses the observed brightness temperatures at 89 GHz (depression in brightness temperature) and thus suppresses the retrieved cloud liquid water (Wang et al., 2005).

The presence of ice at regions of depressed brightness temperature is further confirmed by examining the linear depolarization ratio (LDR), defined as the ratio of the power received in the orthogonal, or cross-polarized, channel to that received in the transmission, or copolarized, channel (Fig. 9). The main component of backscattered signal from cloud droplets has the same polarization as the transmitted polarization, and only large non-spherical particles, such as ice, can change the polarization of the transmitted signal. Thus the high LDR bands around 30, 58, 68, and 143 km are indicative of ice presence there. The locations of these bands are consistent with the bands of brightness temperature depression observed by the MIR. Quantitative retrieval of ice using the depolarization signal is beyond the scope of this paper.

5.2 Retrieval using only the PSR data

The retrieval from the second run (using only the PSR along-track data) shows not only the horizontal variation of clouds but also some vertical structure of clouds (Fig. 8b). The maximum LWC in the retrieval is about 0.5 gm^{-3} and occurs in the 2.0 to 2.8 km altitude range. Adiabatic cloud would have a LWC of about 1–1.4 gm^{-3} at these levels. Thus the maximum LWC in the retrieved cloud field is 30–40% of the adiabatic value. This is consistent with many of the in-situ and remote sensing observations of marine low-level clouds (Albrecht et al., 1990; Miller et al., 1998). The spatial characteristics of the retrieved clouds around the locations of 30, 110, 140 and 160 km are consistent with those in the radar image. The PSR retrieval also reasonably locates some of the

regions with low LWC where the radar reflectivity factors are below −35 dBZ. The cloud top height compares reasonably well with that in the radar image, which is a direct result of the cloud support constraint described in Sect. 3 that forces the retrieval algorithm to produce little or no clouds at altitudes higher than 3.5 km. The regions from 50 to 55 km and from 150 to 155 km where the MIR retrieval incorrectly labels as clear sky are improved in the PSR retrieval, possibly due to less microwave scattering by ice in the 37 GHz frequency than in the 89 GHz frequency. In the region between 58 km and 68 km the radar shows very strong backscattering while the PSR retrieval show very thin clouds or clear sky. We suspect, again, this is due to the strong scattering by ice particles in that region which makes the region appears to be colder and thus reduces the retrieved cloud liquid water content.

5.3 Retrieval using combined MIR and PSR data

For the third run with both the MIR and PSR data, several improvements are noticeable, though, at the first glance, the retrieved distribution of cloud liquid water looks similar to the PSR-based retrieval (Fig. 8c). Around the locations of 35 km and 105 km, the retrieval from the third run shows more consistent cloud structure with the radar image than that from the second run. The gaps between clouds (the regions with low LWC) are better resolved in the combined retrieval than in the PSR-based retrieval. The MIR provides a nadir-viewing measurement every three seconds, while the PSR along-track scans provide a nadir view every 44 s. Thus the addition of the MIR data improves the horizontal structure of the retrieved cloud field.

It should be pointed out that the tomographic data obtained during the Wakasa Bay experiment don't contain enough information to determine cloud structure at high altitudes. We find that, when no cloud support constraint is used, some vertically-uniform puffy clouds appear at high altitudes in the retrieved field, while the radar image shows only clear sky at the same altitudes. These high-altitude clouds are physically implausible because clouds, if present at such high altitudes, would be dominated by ice particles that are almost invisible to centimeter wavelength radiometers. The vertically-

uniform clouds at high altitudes are likely to be caused by the insufficient amount of overlapping between the swaths of successive PSR scan cycles. As shown in Fig. 3, due to the high cruising speed of the NASA P-3 aircraft there is almost no overlapping between the swaths of two successive scans at altitudes higher than 4 km; thus it is difficult for the retrieval algorithm to determine the distribution of cloud water there.

5.4 Liquid water paths calculated from the retrievals

The retrieved LWC fields in the three runs are then integrated along the vertical direction to obtain the corresponding LWP of each column along the flight track. Figure 10a shows the point-by-point comparison between the MIR LWP and the PSR LWP. The correlation coefficient is 0.96. The mean MIR LWP averaged along the flight track also agrees well with that of the PSR in magnitude, suggesting the consistency between the MIR retrieved horizontal structure and the PSR retrieved one. According to Fig. 10a and b, the MIR LWP values are significantly higher than those of the PSR for locations that have thick clouds (LWP>500 gm^{-2}), while, for locations with relatively thin clouds (LWP<150 gm^{-2}), the MIR LWP values are consistently lower than those of the PSR. So the distribution of PSR LWP appears to be much narrower than that of the MIR LWP. There may be several reasons for the narrower distribution of the PSR retrieval. First, the finest scale that the cloud tomography method can resolve depends on the total number of beams and to what extent these beams intersect (Huang et al., 2008a). Beam intersection is determined by the radiometer scanning speed and the platform moving speed for the airborne cloud tomography configuration. Each scan cycle of PSR takes 44 s and during this period the aircraft moves about 5.85 km, resulting in moderate overlapping between two successive scans but very little overlapping between a scan and its second previous scan (Fig. 3). So we expect relatively poor horizontal and vertical resolution for the PSR retrieval. On the other hand, the MIR scanned a 106-degree swath across the flight line every three seconds, producing a nadir measurement every 400 m. Thus the MIR retrieval has a horizontal resolution of about 400 m, although it reveals no vertical structure. Second, the use of regulariza-

tion techniques in the retrieval algorithm, especially the use of smoothness constraint to reduce the high retrieval sensitivity to noise, a typical situation for ill-posed problems, may artificially smooth the horizontal structure in the PSR retrieval.

5.5 Mean difference between measured and calculated brightness temperatures

It is of interest to compare the brightness temperatures with those that can be calculated from the retrieved fields of cloud water content, since this gives a measure of how well the retrieval matches the given microwave brightness temperature data and of how well the guess of liquid water distribution in the adjacent regions matches the observed brightness temperatures. As shown in Sect. 4, we need to guess the cloud liquid water distribution in the two neighboring regions of the retrieval domain, one north-east and the other south-west to the retrieval domain and each 15 km wide, 6.7 km high. We use a subadiabatic profile to approximate the vertical distribution of cloud LWC in these two regions. We then vary the adiabaticity from 0 to 1 and select the one that gives minimum difference between the measured and calculated brightness temperatures as the best guess.

Figure 11a shows the 3-D plot of the mean difference between the simulated and PSR-observed brightness temperatures as a function of the adiabaticity for the aforementioned two neighboring regions. The minimum difference between the two sets of brightness temperatures is 1.9 K; this is comparable with the sum of instrumental noise and uncertainty in the forward modeling of the sea surface brightness temperatures. This minimum is found at an adiabaticity of 0.5 in the northeastern region and 0.25 in the southwestern region. When moving away from the minimum point, the mean difference of brightness temperatures increases smoothly from 1.9 K to 4.1 K. The agreement between the observed and simulated brightness temperatures, of course, does not guarantee the validity of the retrieved liquid water distribution; it only indicates that the retrieval is consistent with the observed brightness temperatures. Figure 11b is a similar plot as Fig. 11a but calculated using only the microwave beams that pass

through either of the two adjacent regions. The minimum difference between the simulated brightness temperatures (for the beams that pass through either of the two regions) and the observed values is 3.3 K and is found at almost the same adiabaticity values as Fig. 11a, i.e., an adiabaticity of 0.5 in the northeastern region and 0.25 in the southwestern region. This agreement suggests that the guess of cloud liquid fields for the two adjacent regions should be close to the truth.

6 Conclusions

This paper examines the results from a limited cloud tomography trial conducted in the Wakasa Bay area as a part of the 2003 AMSR-E validation campaign. During the tomographic experiment, several multi-wavelength microwave radiometers scanned through the nadir along or cross the flight track as the NASA P-3 platform passed a system of boundary layer winter clouds. The geometry of the collected data seems suitable for tomographic retrieval of 2-D cross sections of cloud liquid water content. To handle the highly ill-posed tomographic retrieval problem, we adapt a constrained inversion algorithm that uses different types of constraints to obtain more physically plausible retrievals. Valuable constraints include smoothness, non-negativity, and support constraints (force the retrieval to vanish outside a certain domain). We perform three retrieval runs: one with only the MIR nadir data, one with only the PSR along-track scanning data, and one with the combined PSR and MIR data. The retrieval based on the MIR nadir data, as one would expect, provides only vertically-integrated cloud liquid water and thus no information on the vertical structure is revealed. The PSR retrieval shows physically plausible cloud structure in both horizontal and vertical directions; it not only reasonably captures the locations of clouds but also reasonably reproduces some of the spatial features of cloud water distribution. Combining the PSR and MIR data further improves the retrieval at regions with low cloud water content. When the support constraint is inactivated, some implausible results are identified in the retrieval, e.g., vertically-uniform puffy clouds appear at high altitudes where the

radar image shows clear sky, indicating insufficient information in the data to retrieval cloud structure at such high altitudes.

It is unfortunate that there were no in-situ measurements of cloud water content during the field campaign that can be used to validate the tomographic retrievals. We thus evaluate the retrievals by examining the consistency between the tomographic retrievals and the radar reflectivity image from ACR and by examining the agreement between the calculated LWP from the different retrieval runs. First, we compare the retrievals with the radar reflectivity image obtained by the ACR to qualitatively evaluate how well the tomographic method captures the spatial patterns of clouds. The spatial distribution patterns of cloud water content appear to be consistent with the patterns of radar reflectivity. Second, we calculate the LWP from the retrievals of each retrieval run and compare the PSR LWP and MIR LWP. The PSR LWP correlates with the MIR LWP with a correlation coefficient of 0.96. The mean PSR LWP averaged along the flight track agrees closely with the mean MIR LWP, while the histogram of the PSR LWPs is much narrower than that of the MIR LWPs. Third, we calculate the microwave brightness temperatures in a way consistent with the radiometers observe using known radiometer specifications and the retrieved cloud fields. And we compare the calculated brightness temperatures with the observed values. The mean difference between the calculated and observed brightness temperature is 1.9 K, which is close to the uncertainty associate with the instrumental noises and modeling of the background sea surface emission. Overall, the consistency between the different type of observations shows the usefulness of the cloud tomography approach.

The Wakasa Bay field campaign was designed to provide data for validating the precipitation retrieval algorithms developed for the AMSR-E sensor. As a result, many conditions were not ideal for testing the cloud tomography technique. The NASA P-3 aircraft flew at 144 m/s resulting in insufficient overlapping between successive scan cycles at high altitudes, which eventually leads to ambiguity in the retrievals at these high altitudes. The wind speed was about 20 m/s during the cloud tomography test, causing a 2 to 3 K uncertainty in the background (sea surface) brightness temperatures

and thus causing large uncertainties in the tomographic retrievals. Furthermore, there were no in-situ measurements of cloud water content during the flight to quantitatively evaluate the tomographic retrievals. Nevertheless, this research demonstrates the potential of tomographically retrieving cloud structure using current scanning microwave radiometer technology and identifies several limitations of the airborne cloud tomography test during the Wakasa Bay field campaign. More rigorous sensitivity studies are required to obtain insights by which to improve future field-based studies of cloud tomography. This can be achieved through a suite of complicated field tests that are expensive to implement, or through observation system observation experiments that are much easier and cheaper to implement. The latter is the focus of Part 2 of this paper.

Acknowledgements. This work has been supported by the DOE Atmosphere Radiation Measurement program under Contract DE-AC02-98CH10886. The authors thank Bob Webber of the University of Colorado at Boulder for providing the two-scale sea surface thermal emission model and helping in setting up the model. We are grateful to E. Westwater of the University of Colorado at Boulder for many insightful discussions that help to improve this study. We are grateful to J. Wang of the NASA Goddard Fight Center for providing the MIR data, to R. Austin of Colorado State University for providing the ACR images. We thank E. Lobl University of Alabama in Huntsville for her help in accessing the dropsonde data. It is a pleasure to acknowledge the insightful discussions with Y. Liu and M. Jensen of Brookhaven National Laboratory and G. Liu of Florida State University.

References

Acar, R. and Vogel, C. R.: Analysis of total variation penalty methods, Inv. Prob., 10, 1217–1229, 1994.

Albrecht, B. A., Fairall, C. W., Thomson, D. W., White, A. B., Snider, J. B., and Schubert, W. H.: Surface-based remote sensing of the observed and the adiabatic liquid water content of stratocumulus clouds, Geophys. Res. Lett., 17, 89–92, 1990.

Andersen, A. H. and Kak, A. C.: Simultaneous algebraic reconstruction technique (SART): A superior implementation of the ART algorithm, Ultrason. Imag., 6, 81–94, 1984.

Chambolle, A. and Lions, P. L.: Image recovery via total variation minimization and related problems, Numer. Math., 72, 167–188, 1997.

Corbella, I., Gasiewski, A. J., Klein, M., Leuski, V., Francavilla, A. J., and Piepmeier, J. R.: On-board accurate calibration of dual-channel radiometers using internal and external references, IEEE Trans. Microwave Theory Tech., 50, 1816–1820, 2002.

Frisch, A. S., Fairall, C. W., and Snyder, J. B.: Measurement of stratus cloud and drizzle parameters in ASTEX with a Ka-band Doppler radar and a microwave radiometer, J. Atmos. Sci., 52, 2788–2799, 1995.

Gordon, R., Bender, R., and Herman, G. T.: Algebraic reconstruction techniques (ART) for three-dimensional electron microscopy and X-ray photography, J. Theor. Biol., 29, 471–481, 1970.

Hansen, P. C.: Rank Deficient and Ill-Posed Problems: Numerical Aspects of Linear Inversion, SIAM, Philadelphia, 247 pp., 1998.

Huang, D., Liu, Y., and Wiscombe, W.: Determination of cloud liquid water distribution using 3-D cloud tomography, J. Geophys. Res., 113, D13201, doi:10.1029/2007JD009133, 2008a.

Huang, D., Liu, Y., and Wiscombe, W.: Improving the tomographic retrieval of cloud water distribution using constrained algorithms, J. Geophys. Res., 113, D23203, doi:10.1029/2008JD009952, 2008b.

Johnson, J. T.: An efficient two-scale model for the computation of thermal emission and atmospheric reflection from the sea surface, IEEE Trans. Geosci. Remote Sens., 44, 560–568, 2006.

Lobl, S. E., Aonashi, K., Griffith, B., Kummerow, C., Liu, G., Murakami, M., and Wilheit, T.: Wakasa Bay – an AMSR precipitation validation campaign, B. Am. Meteorol Soc., 88, 551–558, 2007.

Miller, M. A., Jensen, M. P., and Clothiaux, E. E.: Diurnal cloud and thermodynamic variations in the stratocumulus transition regime: A case study using in situ and remote sensors, J. Atmos. Sci., 55, 2294–2310, 1998.

Piepmeier, J. R. and Gasiewski, A. J.: Polarimetric scanning radiometer for airborne microwave imaging studies, Proceedings of International Geoscience and Remote Sensing Symposium, Lincoln, 1688–1691, 1996.

Racette, P. E., Adler, R. F., Wang, J. R., Al Gasiewski, Jackson, D. M., and Zacharias, D. S.: An airborne millimeter wave imaging radiometer for cloud, precipitation, and atmospheric water vapor studies, J. Atmos. Ocean. Tech., 13, 610–619, 1996.

Ramanathan, V., Cess, R., Harrison, E., Minnis, P., Barkstrom, B., Ahmad, A., and Hartmann, D.: Cloud-radiative forcing and climate: results from the earth radiation budget experiment, Science, 243, 57–63, 1989.

Sadowy, G., McIntosh, R., Dinardo, S., Durden, S., Edelstein, W., Li, F., Tanner, A., Wilson, W., Schneider, T., and Stephens, G.: The NASA DC-8 airborne cloud radar: design and preliminary results, Proceedings of International Geoscience and Remote Sensing Symposium, Singapore, 1997.

Sezan, M. I. and Stark, H.: Image restoration by the method of convex projections: Part 2 – Applications and numerical results, IEEE Transact. Med. Imag., MI-1, 95–101, 1982.

Sezan, M. I. and Stark, H.: Image restoration by convex projections in the presence of noise, Appl. Opt., 22, 2781–2789, 1983.

Sidky, E. Y. and Pan, X.: Image reconstruction in circular cone-beam computed tomography by constrained total-variation minimization, Phys. Med. Biol., 53, 4777–4807, 2008.

Strong, D. and Chan, T. F.: Edge-preserving and scale-dependent properties of the total variation regularization, Inv. Prob., 19, 165–187, 2003.

Twomey, S.: Introduction to the mathematics of inversion in remote sensing inversion and indirect measurements, Elsevier, Amsterdam, 243 pp., 1977.

Wang, J., Racette, P., Austin, R. T., Liu, G. S., and Sekelsky, S. M.: Remote Measurements of Snowfalls in Wakasa Bay, Japan with Airborne Millimeter-wave Imaging Radiometer and Cloud Radar, Proceedings of IEEE International Geoscience and Remote Sensing Symposium, Anchorage, Alaska, 2004.

Warner, J., Drake, J. F., and Krehbiel, P. R.: Determination of cloud liquid water distribution by inversion of radiometric data, J. Atmos. Ocean. Tech., 2, 293–303, 1985.

Warner, J., Drake, J. F., and Snider, J. B.: Liquid water distribution obtained from coplanar scanning radiometers, J. Atmos. Ocean. Tech., 3, 542–546, 1986.

Youla, D. C. and Webb, H.: Image restoration by the method of convex projections: Part 1 – Theory, IEEE Transact. Med. Imag. MI-1, 81–94, 1982.

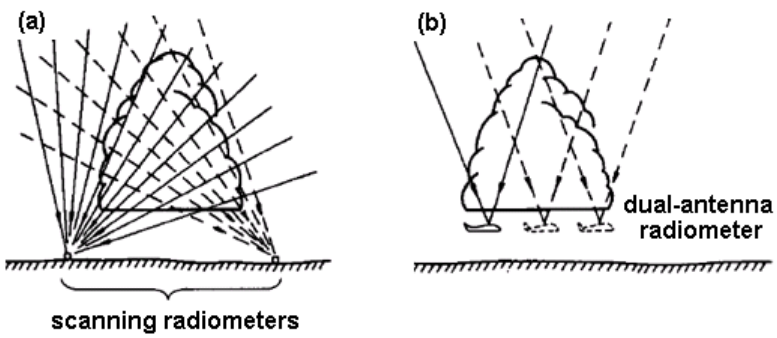

Fig. 1. Two cloud tomography configurations presented in Warner et al. (1985). **(a)** A ground-based configuration with two distinctly-located scanning radiometers; **(b)** an air-borne configuration with two fixed microwave antennas.

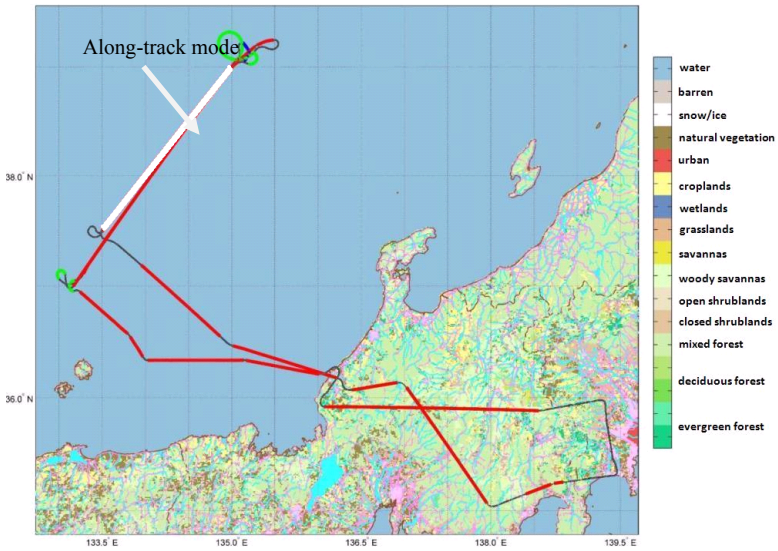

Fig. 2. Flight tracks of the NASA P-3 aircraft on 28 January 2003 over the Sea of Japan. White – the flight path where PSR was operating on the along-track mode (the only mode suitable for cloud tomography retrieval); Red – data collected with PSR/A flown in a straight and level line; Green – data collected with PSR flown in a constant angle turns.

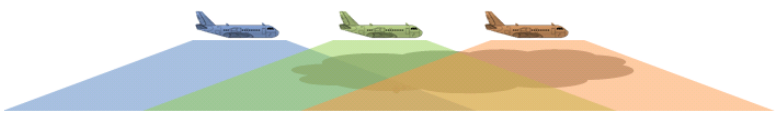

Fig. 3. Schematic of the geometry of the PSR along-track scans. The cartoon shows the swaths of three successive scan cycles, each labeled in different color. Each PSR swath spans ±70 degrees off the nadir. The aircraft translates approximately 5.85 km during a full PSR scan cycle. It can be seen from the cartoon that a scan cycle moderately overlaps with its succeeding scan, but hardly overlaps with its second succeeding scan.

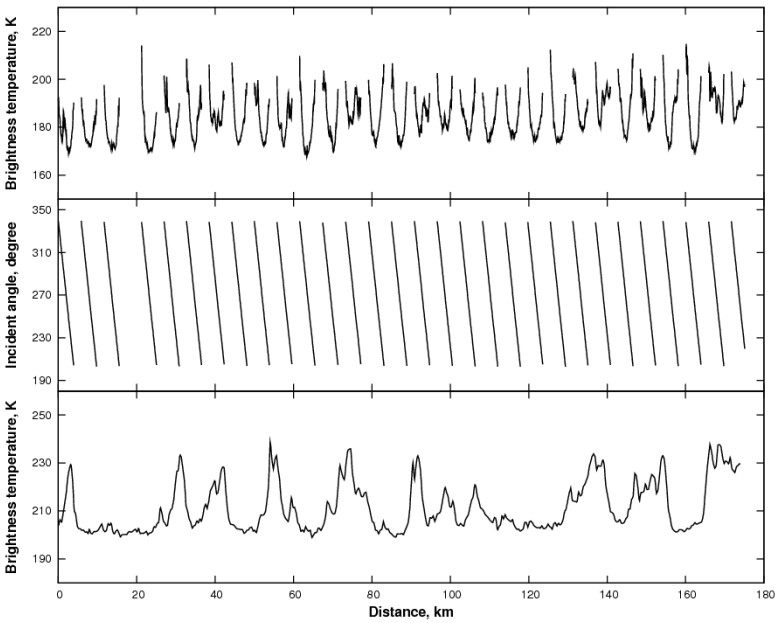

Fig. 4. Examples of radiometric data obtained from the PSR and MIR aboard the NASA P-3 research aircraft during the Wakasa Bay AMSR-E validation campaign. **(a)** The PSR brightness temperature as a function of distance; **(b)** the corresponding viewing angle; **(c)** the MIR nadir-viewing brightness temperature. The PSR scanned within ±70 degrees off the nadir along the flight line, providing multi-angular measurements of microwave emission in the vertical plane of the flight track. The MIR was programmed to scan within 106-degree swath across the flight track and only the nadir-viewing measurements are used in this study.

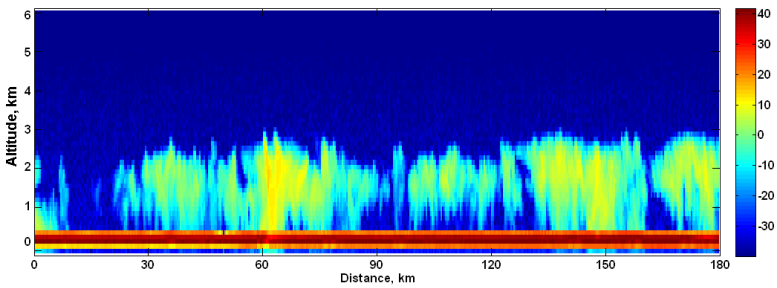

Fig. 5. The image of co-polarization radar reflectivity factor obtained by the ACR. The high values (>30 dBZ) around the surface correspond to the sea surface returns. Below the sea surface, no radar return is allowed. But multiple scattering of microwave between clouds and the sea surface makes the involved radar returns appear to be from below the sea surface.

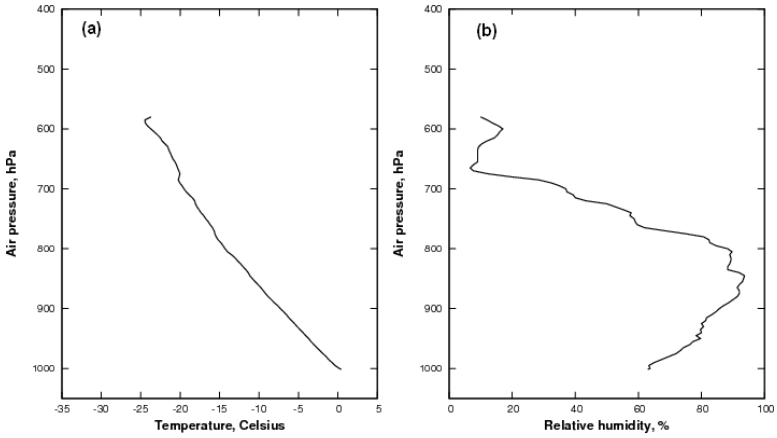

Fig. 6. The mean profiles of air temperature **(a)** and relative humidity **(b)** obtained from three dropsondes launched during the flight.

- 1. $\mathbf{x}_0=\mathbf{x}$
- 2. SART //Enforce data constraint
- 3. $\bullet b=|\mathbf{Ax}-\mathbf{b}|$, $\bullet x_{data}=|\mathbf{x}-\mathbf{x}_0|$ //the change due to data constraint
- 4. if ($x(r)<0$) $x(r)=0$ //enforce non-negativity constraint
- 5. if ($r\notin \mathbf{L}$) $x(r)=0$ //enforce support constraint
- 6. $\mathbf{x}_0=\mathbf{x}$
- 7. Total variation steepest descent with step size d_{TV}
- 8. $\bullet x_{TV}=|\mathbf{x}-\mathbf{x}_0|$ //the change due to total variation steepest descent steps
- 9. $d_{data}=0.99*d_{data}$
- 10. if ($\bullet b<\varepsilon$ and $\bullet x_{TV}>\bullet x_{data}$) $d_{TV}=0.95*d_{TV}$
- 11. if (stop criteria) return; else go to step 1.

Fig. 7. The pseudo-code of the constrained retrieval algorithm. The constraints implemented in the retrieval algorithm include smoothness, non-negativity, and support constraints.

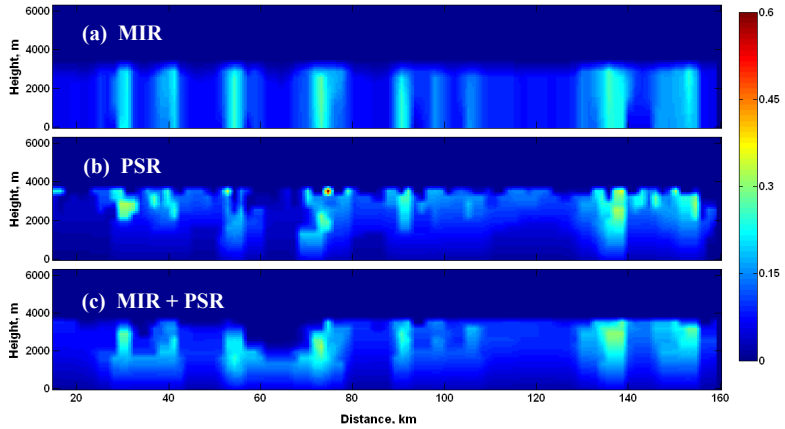

Fig. 8. Retrieved cloud liquid water fields using the MIR data, the PSR data, and the combination of MIR and PSR data.

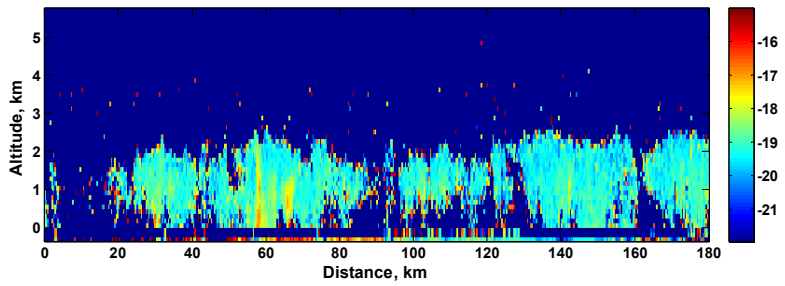

Fig. 9. The image of linear depolarization ratio (LDR) obtained by the ACR. The most probable value of LDR inside the clouds is −19.2 dB, while bands of higher LDR are also found around locations at 30, 58, 68, and 143 km. These high LDR bands are indicative of non-spherical ice particles which can change the polarization of scattered microwave. Nevertheless, quantitative retrieval of ice from the LDR data is difficult in this case because the LDR signal is very week (only 1–1.5 dB).

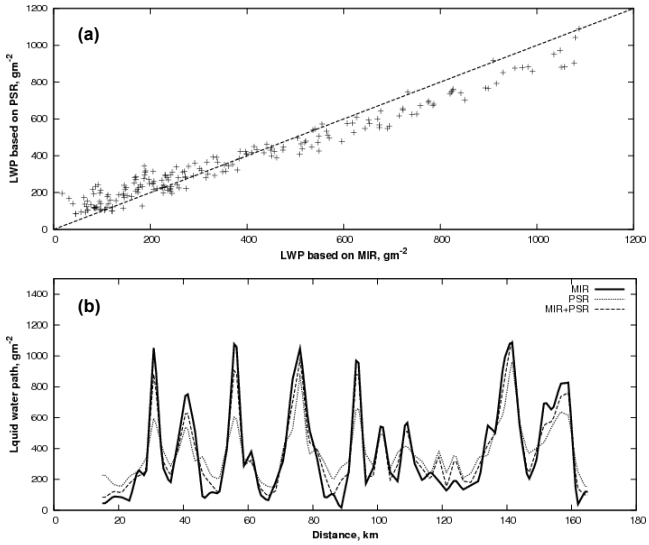

Fig. 10. Comparison of the liquid water paths based on the MIR and PSR data. **(a)** scatter plot; **(b)** liquid water paths as a function of distance.

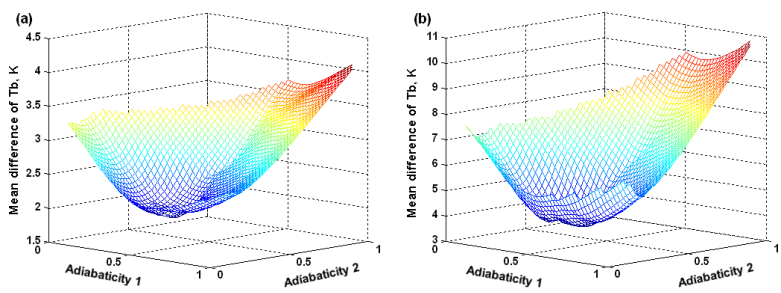

Fig. 11. The mean differences between the simulated and observed brightness temperature as a function of the adiabaticity at the two regions adjacent to the retrieval domain. **(a)** For beams that strike through either of the two adjacent regions; **(b)** for all beams.